INTRODUCTION

1.1 THE AGN-HOST GALAXY CONNECTION

Super-massive black holes (BHs) are found at the centres of most nearby massive galaxies and the BH mass and mass of the host galaxy spheroid are strongly correlated (Ferrarese and Merritt, 2000; Gebhardt et al., 2000; Kormendy and Ho, 2013). Although any underlying causal mechanism(s) responsible for the correlation is yet to be conclusively identified, there is considerable observational and theoretical support for models that involve BH-fuelling, outflows and a 'feedback' relationship (e.g. King and Pounds, 2015). The number density of quasars, which evolves strongly with redshift, peaks at redshifts $2 \lesssim z \lesssim 3$ (e.g. Brandt and Hasinger, 2005; Richards et al., 2006b) and the most massive ($M_{BH} \gtrsim 10^9 M_\odot$) present-day BHs experienced much of their growth during this epoch. The star formation rate, which closely follows the cosmological evolution of the quasar luminosity function, also peaks during this epoch (e.g. Boyle and Terlevich, 1998). Quantifying the growth-rate of massive BHs at $2 \lesssim z \lesssim 3$ would therefore help significantly in understanding the role quasars play in galaxy evolution.

There is now considerable observational and theoretical support for models of galaxy formation that involve black hole-fuelling, outflows and a 'feedback' relationship between active black holes and star formation in the host galaxy. Super-massive black holes accreted most of their mass and galaxies formed most of their stars at redshifts $z \gtrsim 2$ (e.g. Madau & Dickinson 2014 for star formation; find quasar reference.) During this key cosmological epoch star formation is believed to be suppressed by the energy output from the quasar, establishing the tight relationship between BH mass and host galaxy spheroid mass observed in the local Universe (e.g. Kormendy & Ho 2013).

1.2 MEASURING BLACK HOLE MASSES

The goal of better understanding the relationship between super-massive BH accretion and star formation has led to much work focussing on the properties of quasars and active galactic nuclei at these redshifts. Accurate BH mass estimates for quasars are essential in these studies. Furthermore, as one of just two fundamental quantities describing a black hole on astrophysical scales, the mass is of crucial importance

to virtually all areas of quasar science, including the evolution and phenomenology of quasars, and accretion physics.

1.2.1 *Reverberation Mapping*

Reliable estimates of BH masses are a prerequisite for investigating the relationship between BHs and their host galaxies. If the line-emitting clouds in the broad line region (BLR) are assumed to be virialized and moving in a potential dominated by the central BH, then the BH mass is simply a product of the BLR size and the square of the virial velocity. The reverberation-mapping technique uses the time lag between variations in the continuum emission and correlated variations in the broad line emission to measure the typical size of the BLR (Peterson, 1993; Peterson, 2014). The full width at half maximum (FWHM) or dispersion (σ; derived from the second moment) velocity of the prominent broad emission line of Hβ (4862.7Å)[1] is used as an indicator of the virial velocity, with extensions to other low-ionization emission lines such as Hα (6564.6Å) and Mg II$\lambda\lambda$2796.4,2803.5 (e.g. Vestergaard, 2002; McLure and Jarvis, 2002; Wu et al., 2004; Kollmeier et al., 2006; Onken and Kollmeier, 2008; Wang et al., 2009; Rafiee and Hall, 2011). Extensive reverberation mapping campaigns have provided accurate BH masses for ~50 active galactic nuclei (AGN) at relatively low redshifts and of modest luminosity (e.g. Kaspi et al., 2000; Kaspi et al., 2007; Peterson et al., 2004; Bentz et al., 2009; Denney et al., 2010). [See galaxies talk for a few more details]

1.2.2 *Single-Epoch Virial Estimates*

Reverberation mapping campaigns have also revealed a tight relationship between the radius of the BLR and the quasar optical (or ultraviolet) luminosity (the $R - L$ relation; e.g. Kaspi et al., 2000; Kaspi et al., 2007). This relation provides a much less expensive method of measuring the BLR radius, and large-scale studies of AGN and quasar demographics have thus become possible through the calibration of single-epoch virial-mass estimators using the reverberation-derived BH masses (e.g. Greene and Ho, 2005; Vestergaard and Peterson, 2006; Vestergaard and Osmer, 2009; Shen et al., 2011; Shen and Liu, 2012; Trakhtenbrot and Netzer, 2012). The uncertainties in reverberation mapped BH masses are estimated to be ~ 0.4 dex (e.g. Peterson, 2010), and the uncertainties in virial masses are similar (e.g. Vestergaard and Peterson, 2006). Since the structure and geometry of the BLR is unknown, a virial coefficient f is introduced to transform the observed line-of-sight velocity inferred from the line width in to a virial velocity. This simplification accounts for a significant part of the uncertainty in virial BH masses (in addition to, for example, describ-

---

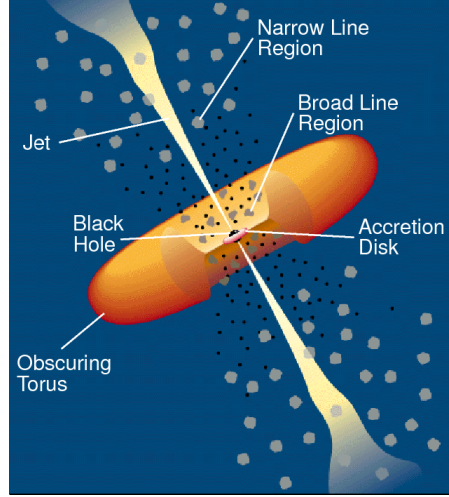1 Vacuum wavelengths are employed throughout the thesis.

Figure 1.1: Illustration of the physical structure of an AGN in a simple orientation-based unification model. From Urry and Padovani, (1995).

ing the BLR with a single radius R and scatter in the R − L relation; Shen, 2013). Furthermore, if the BLR is anisotropic (for example, in a flattened disk; e.g. Jarvis and McLure, 2006) then the line width will be orientation-dependent (e.g. Runnoe et al., 2013; Shen and Ho, 2014; Brotherton et al., 2015).

For example, single epoch estimates have been used to calculate black hole masses in the highest redshift quasars to study the growth of SMBHs. This figure shows a compilation of SE mass estimates for quasars over a wide redshift range from different studies. These studies show that massive, 10^9 BHs are probably already in place by $z \sim 7$, when the age of the Universe is less than 1 Gyr. This places strong constraints on BH growth models. Single epoch masses have also been used to study the distribution of quasars in the BH mass-luminosity plane, which conveys important information about the accretion process of these active black holes (e.g. Kollmeier et al. 2016). Reshift evolution of BH-bulge scaling relations (e.g. Bennert et al. 2011). Clustering (Shen & Ho 2014; Timins et al.?).

An *active galactic nucleus*, or AGN, is an energetic, non-stellar phenomena in the central region of a galaxy. AGN are powered by the accretion of gas, primarily through an accretion disk, onto a central *super-massive black hole* (SMBH) of mass 10^{6-9} M$_\odot$ (Lynden-Bell, 1969). With bolometric luminosities in the range 10^{44-48} ergs^{-1}, they are the most luminous persistent sources of radiation in the Universe.

1.3 ORIENTATION-BASED UNIFICATION MODELS

AGNs are divided into numerous classes and sub-classes based on their observational properties. AGN unification models (Antonucci,

; Urry and Padovani,) attempt to explain the diversity in their observational properties using as few physical parameters as possible. In many unification models the optical and radio luminosities are considered to be intrinsic parameters. Variations in the radio luminosity explains the difference between the $15 - 20\%$ of AGN which are *radio-loud* (i.e. have radio to optical flux ratios $\gtrsim 10$) and the remainder which are *radio-quiet*. The optical luminosity explains, for example, the difference between low-luminosity *Seyfert Galaxies* and high-luminosity *quasars*[2]. In a typical quasar the optical emission may be brighter than the combined emission from all of the stars in the host galaxy by a factor of 100 or more. The large brightness contrast between the nucleus and the host galaxy makes the host galaxy difficult to detect, and the quasar is observed as an unresolved stellar-like object[3].

Unification models attempt to explain all further observational differences as being apparent differences due to *orientation* effects. The basic physical structure of an AGN in this model is illustrated in Figure 1.1. Material is pulled towards the SMBH at the centre and sheds angular momentum through viscous and turbulent processes in an accretion disk, which radiates primarily at ultraviolet (UV) to soft-X-ray wavelengths. Strong optical and UV emission lines are produced in photo-ionised gas clouds moving rapidly in close proximity to the SMBH. The doppler-broadened emission line widths imply gas cloud velocities of thousands of km s^{-1} in this *broad-emission line*. Further out are dusty, molecular clouds, the geometry of which is often modelled as a torus co-planar with the accretion disk. Along some lines of sight from the observer to the accretion disk / broad line region the dusty torus obscures the UV/optical radiation. In this case, an observer would see a weak UV/optical continua and no broad emission lines and classify the AGN as being *Type II*. On the other hand, if the line of sight is unobscured by the dusty torus then a broad emission line component would be observable in the spectrum and the AGN would be classified as being *Type I*. Further away from the central black hole and beyond the dusty torus are slower moving clouds of gas which are photo-ionised by the continuum emission from the accretion disk and produce forbidden emission lines of narrower widths (typically hundreds of km s^{-1}). Outflows of energetic particles occur along the poles of the accretion disk and form collimated radio-emitting jets and in some cases giant radio-emitting lobes. A strong, relativistically beamed component with large variations in brightness on very short timescales (e.g. $\Delta m \gtrsim 0.1$ and $\Delta t \lesssim 1$

---

2 The term 'quasar' is sometimes reserved for radio-loud objects and 'quasi-stellar object', or 'QSO', for radio-quiet objects. Here, 'quasar' is used to refer to all luminous AGN.

3 The name 'quasar' is shortened from 'quasi-stellar radio source', since quasars were originally discovered as optical point-source counterparts to a newly discovered population of radio sources.

day) is observed and a source with these properties is classified as a *blazar*.

While an orientation-based unification scheme such as this is somewhat successful at explaining many of the observational properties of AGNs, other factors such as the host galaxy morphology and gas/dust content may also be important (Peterson, 1997). It is also doubtful whether the geometry of the dusty torus is the same in all AGNs, and the fraction of obscured quasars has been shown to decrease with increasing nuclear luminosity (Lawrence, 1991). As we will now discuss, quasars might play an important role in a broader cosmological context, affecting the formation and evolution of the galaxies, groups, and clusters in which they reside. In this scenario of galaxy/quasar co-evolution the quasar is expected to transition from a highly active obscured phase to an unobscured phase as it clears out the dust surrounding it. If this picture is true then we should expect to find variations in the observational properties of the quasar and host galaxy as the system transitions through the different stages of its evolution.

1.4 THE TORUS

Elitzur & Shlosman (2006):

Recent high-resolution IR observations indicate that the torus size might be no more than a few parsecs (Elitzur 2005 and references therein); in particular, VLTI observations of NGC 1068 show that the FWHM size of the 12 mm emission is only 4 pc (Jaffe et al. 2004). The compact sizes place the torus inside the region where the SBH gravity dominates over the galactic bulge.

Two approaches have been taken for the torus dynamic origin. A hydrostatic scenario depicts the torus as a doughnut-like structure populated by molecular clouds accreted from the galaxy (Krolik & Begelman 1988). However, the origin of vertical mo tions capable of sustaining the clouds in a hydrostatic structure with H~R was recognized from the start as problematic and has eluded solution thus far (e.g., Davies et al. 2006). The other scenario, based on the seminal work by Blandford & Payne (1982), involves the outflow of clouds embedded in a hydromagnetic disk wind (Emmering et al. 1992, hereafter EBS92; Konigl & Kartje 1994; Kartje & Konigl 1996; Bottorff et al. 1997, 2000; Kartje at al. 1999; Everett 2005). In this approach the torus is merely a region in the wind that happens to provide the required toroidal obscuration; i.e., it is that region wherein the clouds are dusty and optically thick.

1.5 EVOLUTIONARY MODELS

A number of observations link the growth and evolution of quasars to the growth and evolution of galaxies. These include the following:

1. SMBHs appear to be a ubiquitous feature at the centres of all massive galaxies (e.g. Kormendy and Ho, 2013).

2. SMBH masses are proportional to the mass/velocity dispersion of their host spheroid (the $M - \sigma$ relation; Ferrarese and Merritt, 2000; Gebhardt et al., 2000).

3. The cosmological evolution of the star formation rate and the quasar luminosity function are very similar (e.g. Wall et al., 2005).

4. Cosmological simulations of galaxy formation and evolution require feedback from SMBH growth in order to reproduce the galaxy luminosity function (Kauffmann and Haehnelt, 2000).

These observations suggest that all galaxies may have gone through a 'quasar phase' during which the SMBH accretes most of its mass and the stellar-bulge forms most of its stars. This evolutionary phase could be triggered by a major merger or by instabilities in the galactic disc or bulge. In a galaxy merger large amounts of gas can shed sufficient angular momentum to settle into dense clouds and form stars or be funnelled to the centre of the galaxy to grow the existing SMBH. The large amounts of gas and dust funnelled inward to the galactic nucleus is predicted to obscure the quasar until the dust is cleared out either by quasar-driven or stellar-driven processes. An unobscured quasar then emerges, and is active until all of the available material has been accreted (Hopkins et al., 2006; Narayanan et al., 2010). The feedback processes involved are also thought to be responsible for shutting down star formation in the galactic bulge (Silk and Rees, 1998) and establishing the $M - \sigma$ relation.

Such scenarios have been invoked to explain the presence of buried AGN seen in ultra-luminous infra-red galaxies (ULIRGs; Sanders et al., 1988), a high fraction of which also show evidence of merging and interaction. However, the full picture is likely to be more complicated. Although there is evidence that mergers dominate at high luminosities (Treister et al., 2012), stochastic accretion may be more important at low luminosities (e.g. Hopkins and Hernquist, 2006).

Luminous unreddened quasars show few signs of interaction (e.g. Dunlop et al., 2003) which, if the quasar-galaxy co-evolution model is true, suggests that indications of an interaction disappear during a transitional phase. Quasars in this transitional phase would be highly reddened, as the dust enshrouding the nucleus will not have been fully cleared, but not completely obscured. A population of quasars with these properties may therefore represent a link between ULIRGs and unobscured quasars.

1.6.1 *Red and Reddened Quasars*

Magnitude limited optical surveys of quasars are biased against selecting red and reddened quasars. Richards et al., (2003) studied a large sample of optically selected Sloan Digital Sky Survey (SDSS; York et al., 2000) quasars and showed the mean reddening to be $E(B-V) = 0.03$ at the redshift of the quasar. They estimated that $\sim 15\%$ of the population was missing from the survey due to dust extinction. The missing fraction, and it's dependence on luminosity and redshift, could help to determine whether the reddened population is best explained in the context of orientation-based unification models with non-spherical geometry or as an evolutionary stage in a quasars lifetime.

Populations of heavily dust-reddened quasars have been identified using radio surveys (e.g. Glikman et al., 2012), by using the 'K-band excess' in the spectra of quasars relative to stars (Maddox et al., 2012), and using near-IR colour selection (Banerji et al., 2012; Banerji et al., 2013). Recently, Ross et al., (2014) identified a small sample of very red SDSS quasars based on their extreme IR to optical luminosity ratios. It is yet to be determined whether these extreme objects are simply the tail of a population dominated by less reddened quasars, or whether the distribution is bi-modal with reddening. A population of quasars with intermediate amounts of dust reddening $(0.1 \lesssim E(B-V) \lesssim 0.5)$ would help to address this question.

1.6.2 *Broad Absorption Line Quasars*

Broad absorption line quasars (BALQSOs) are a sub-population of quasars exhibiting blue-shifted absorption troughs broader than 2000kms^{-1} (Weymann et al., 1991) which are unambiguously associated with AGN-driven out-flowing gas. As well as showing high rates of mergers, an anomalously large fraction of heavily reddened objects exhibit broad blue-shifted absorption troughs in their spectra (Urrutia et al., 2009; Glikman et al., 2012). This observation suggests that the BAL phenomenon may be related to a 'blow-out' phase of a quasars lifetime as it transitions from a dusty, obscured objected to a luminous blue quasar, at the same time quenching star formation. Since outflows are believed to be fundamental to AGN feedback, a better understanding of their properties could shed light on the outflow phenomenon. Alternatively, whether a quasar is observed to have broad absorption lines could depend only on the orientation of the observer in relation to an intrinsically anisotropic system.

1.6.3 *Hot-Dust-Poor Quasars*

The near-IR emission from AGN is generally explained by thermal emission from dust grains at the edge of the dusty torus closest to the accretion disk. The dust is heated to its sublimation temperature (1300-2000K Barvainis, 1992) by emission from the accretion disc. However, Hao et al., (2010) reported that 6% (at $z \lesssim 2$) to 20% (at $2 \lesssim z \lesssim 3.5$) of the quasars in the X-ray selected XMM-COSMOS Type 1 AGN sample (Brusa et al., 2010) have an unusually small amount of hot dust emission, despite having normal accretion disc spectra. They infer a torus covering factor of ~2% to 30% for these 'hot dust poor' (HDP) quasars, well below the ~75% predicted by unified models (e.g. Krolik and Begelman, 1988). Hao et al., (2011) found that HDP quasars were just as common in the Richards et al., (2006a) Spitzer/SDSS sample (8.7% $\pm$ 2.2%) and the Elvis et al., (1994) Palomar-Green-quasar-dominated sample (9.5% $\pm$ 5.0%). Either the hot dust is destroyed (dynamically or by radiation), or the dust is not centred on the SMBH, which could happen during a major merger (e.g. Blecha et al., 2011). Alternatively, misaligned accretion disks, which will result from discrete isotropic accretion events (Volonteri, Sikora, and Lasota, 2007), will lead to a wider range of covering factors (Lawrence and Elvis, 2010).

At higher redshifts, Jiang et al., (2010) found two HDP quasars in a sample of 21 at $z \sim 6$. They find that at $z \sim 6$ the hot dust abundance is roughly proportional to the black hole mass, indicating that the two grow at about the same rate. The two HDP quasars also have the smallest SMBH masses, and may be too young to have formed a significant amount of hot dust.

1.6.4 *Type II Quasars*

As well as lacking a broad-line spectral component, Type II AGN tend to have high IR to optical light ratios, hard X-ray spectra, and be strongly polarised, consistent with dusty torus based unification schemes. The detection of unobscured continuum emission that is scattered and polarised by dust above the torus has confirmed the orientation-based unification of Type I and Type II Seyfert Galaxies. Their higher luminosity analogues, Type II quasars, have been much more difficult to detect and study. It is possible that the orientation-based Type I/II unification scheme may break down at high-luminosities, and that instead all quasars could pass through a Type II phase before the obscuring dust is cleared out by the quasar-driven outflows and a Type I quasar emerges.
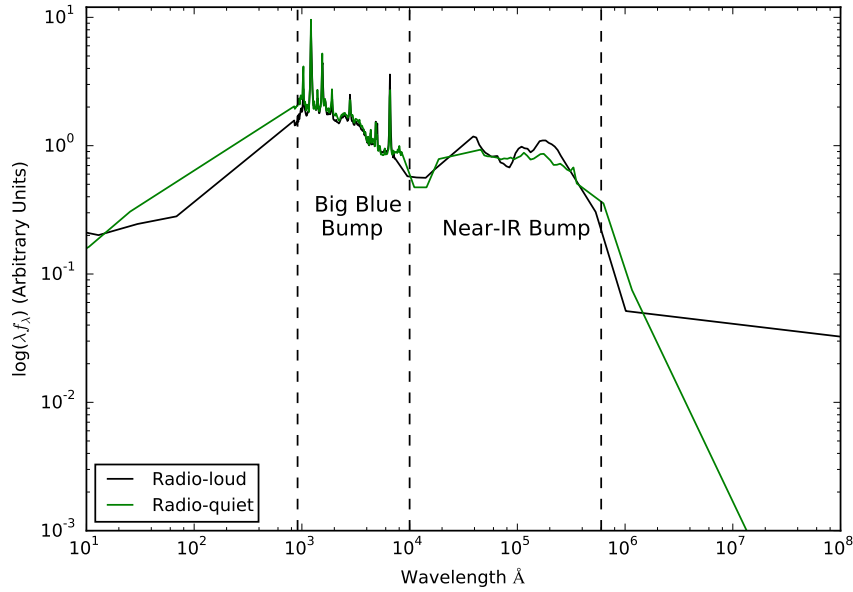
Figure 1.2: Median SEDs for radio-loud and radio-quiet quasars from Shang et al., (2011).

1.7 SPECTRAL ENERGY DISTRIBUTIONS

AGNs emit strongly over many decades in frequency of the electromagnetic spectrum and the energy emitted as a function of frequency is described by a *spectral energy distribution* (SED). As we will describe below, the broad features in the SED originate from processes which occur in different regions of the AGN. In the preceding sections, we have described how some interesting sub-populations of AGNs might relate to the broader population in the context of orientation-based unification schemes and evolutionary schemes. Comparing SEDs of different sub-populations can help to shed light on these relationships and the physical processes which drive them. Possible correlations between the SED shape and luminosity, redshift, and other properties of the AGN such as black hole mass and Eddington ratio can also constrain models of AGN structure and evolution.

Since the physical processes involved are generally understood only qualitatively, almost all AGN SED templates are empirical. The empirical template of Elvis et al., (1994), constructed using photometric observations from the radio to the hard X-rays of 29 radio-quiet and 18 radio-loud Type I quasars, is still the most commonly cited, despite many additions and updates (e.g. Polletta et al., 2000; Kuraszkiewicz et al., 2003; Risaliti and Elvis, 2004; Richards et al., 2006a; Polletta et al., 2007; Lusso et al., 2010; Shang et al., 2011; Marchese et al., 2012; Trichas et al., 2012). In Figure 1.2 we show the median spectrum from the radio-loud and radio-quiet samples of Shang et al. (2011). Short-

9

ward of the radio region, the radio-loud and radio-quiet spectra are almost indistinguishable.

A large amount of energy is emitted in the UV/optical region short-ward of ~ 4000Å: the *Big Blue Bump*. In the X-ray region, the *soft X-ray excess* may be the high-energy end of this feature. The Big Blue Bump is generally attributed to thermal emission from the accretion disk. In Type II AGNs, the continuum emission from the accretion disk is obscured, and so the Big Blue Bump in the SED of a Type II AGN would be less prominent than is seen in Figure 1.2.

The feature at wavelengths long-ward of $\sim 1\mu$m is the *IR Bump*, and is generally attributed to thermal emission from dust at a wide range of temperatures ($\sim 50 - 1000$ K). The amount, geometry, ionisation and optical depth of absorbing dust and gas and its inclination determines the shape of the IR Bump and the absorption of the optical/UV continua. The relative strengths of the IR Bump and the Big Blue Bump are generally comparable, although they do vary from object to object. In particular, for the HDP objects we described above the IR Bump appears to be missing entirely. The minimum between the two peaks is at $\sim 1\mu$m, which reflects the sublimation of dust at T $\gtrsim 2000$ K (Sanders et al., 1989).

Emission in the hard X-ray region of the spectrum is believed to be due to Compton up-scattering of accretion disk photons by hot electrons forming a corona in the vicinity of the disk (e.g. Sunyaev and Titarchuk, 1980). The radio emission, which originates from synchrotron emission in relativistic jets, contributes very little to the total energy output. However, the mechanical energy provided by the jets is an important component of AGN feedback models (e.g. Fabian, 2012).

Many parameters might be expected to affect the shape of the AGN SED (e.g. the black hole mass, the accretion rate, the physical properties of the accretion disk, the properties of the absorbing dust) and many of these properties might be expected to change as the quasar evolves (e.g. as dust is expelled from the nuclear regions). Given this, it is perhaps surprising that many authors have found no significant dependence of the mean SED on properties such as redshift, bolometric luminosity, SMBH mass, or accretion rate (e.g. Elvis et al., 2012; Hao et al., 2013) and that quasars up to redshift 7 have been shown to have similar UV spectra to low redshift quasars (e.g. Mortlock et al., 2011).

Throughout this thesis we adopt a ΛCDM cosmology with $h_0 = 0.71$, $\Omega_M = 0.27$, and $\Omega_\Lambda = 0.73$. All wavelengths and equivalent width measurements are given in the quasar rest-frame, and all emission line wavelengths are given as measured in vacuum.

Everett et al. (2005):

A variety of observational signatures point to the importance of outflowing gas within many types of active galactic nuclei (AGNs).

Blueshifted absorption features (in broad absorption line quasars, or BALQSOs; see, e.g., Weymann et al. 1991) are seen in approximately 15% (Reichard et al. 2003) of radio-quiet quasars, with velocities up to 0.1c. In addition, radio-loud quasars display relativistic, collimated outflows. There has also been observational evidence that suggests the mass outflow rate in AGNs is nearly equal to the mass inflow rate (see, e.g., Crenshaw et al. 2003; Chartas et al. 2003).

SED PROPERTIES

While many authors have focused on studies of specific sub-sets of active galactic nuclei (AGN) with extreme observational properties, what is missing is an understanding of how these extreme subsets relate to the population as a whole. I have addressed this problem using multi-wavelength spectral energy distributions (SEDs) of large samples of quasars. I have constructed an SED model which is able to reproduce the average optical to near-infrared (NIR) colours of 10,000s of AGNs spanning a broad range in redshift and luminosity.

2.1 DATA

The systematic study of the dependence of the SED shape on physical parameters has, until very recently, been limited by the difficulty in obtaining a large sample of quasars with good multi-wavelength coverage and large dynamic range in luminosity and redshift. In this work, we take advantage of a number of recent, sensitive, wide-field surveys, covering the UV to mid-IR spectral region.

2.1.1 *The Sloan Digital Sky Survey*

We use the Seventh Data Release (DR7) of the Sloan Digital Sky Survey (SDSS; York et al., 2000) spectroscopic quasar catalogue (Schneider et al., 2010), which includes 105,783 objects across 9380 deg^2. The SDSS obtained images in five broad optical passbands: u ($\lambda_{eff} = 3543$Å), g ($\lambda_{eff} = 4770$Å), r ($\lambda_{eff} = 6231$Å), i ($\lambda_{eff} = 7625$Å), and z ($\lambda_{eff} = 9134$Å). We use BEST point-spread function (PSF) magnitudes, correcting for Galactic extinction using the maps of Schlegel, Finkbeiner, and Davis, (1998), assuming a Milky Way (MW) extinction curve (Pei, 1992) and an extinction to reddening ratio $A(V)/E(B-V) = 3.1$. Although the SDSS asinh magnitude system is intended to be on the AB system (Oke and Gunn, 1983), the photometric zeropoints are known to be slightly off the AB standard. To account for this we add 0.03 mag to the u, g, r and i magnitudes, and 0.05 mag to the z magnitude.

Where did these numbers come from?

DR7Q quasar targets were primarily selected to have $i \leqslant 19.1$ if the colours were consistent with being at redshift $z < 3$, and $i \leqslant 20.2$ if consistent with $z > 3$ (Richards et al., 2002). The survey is sensitive to the most luminous quasars at a given redshift. The large number of objects at $z < 3$ with $i > 19.1$ were selected by algorithms other than the main quasar selection. For example, quasar targets were also

selected if they matched within $2''$ of an object in the Faint Images of the Radio Sky at Twenty-cm (FIRST) catalogue of radio sources (Becker, White, and Helfand, 1995).

2.1.2 *UKIDSS Large Area Survey*

We use the UKIRT Infrared Deep Sky Survey (UKIDSS; Lawrence et al., 2007) Large Area Survey (ULAS) which has observed $\sim 3,200$ deg^2 in four near-IR passbands: Y ($\lambda_{eff} = 1.0305\mu m$), J ($\lambda_{eff} = 1.2483\mu m$), H ($\lambda_{eff} = 1.6313\mu m$), and K ($\lambda_{eff} = 2.2010\mu m$)). We used the ninth data release (DR9) of the ULAS. Cross-matching (with a $2''$ radius and picking only the nearest neighbour) the SDSS DR7Q catalogue with the ULAS catalogue, which covers only $\sim 38\%$ of the SDSS footprint, resulted in 37,893 matches. The ULAS magnitudes are aperture corrected magnitudes in a $2''$ diameter aperture and are not corrected for Galactic extinction.

2.1.3 *WISE All-WISE Survey*

The Wide-field Infrared Explorer (WISE; Wright et al., 2010) mapped almost the sky in four mid-IR band-passes: $W1$ ($\lambda_{eff} = 3.4\mu m$), $W2$ ($\lambda_{eff} = 4.6\mu m$), $W3$ ($\lambda_{eff} = 12\mu m$), and $W4$ ($\lambda_{eff} = 22\mu m$). The WISE AllWISE Data Release ('AllWISE') combines data from the nine month cryogenic phase of the mission that led to the 'AllSky' data release with data from the NEOWISE program (Mainzer et al., 2011). Cross-referencing the SDSS DR7Q catalogue with the AllWISE catalogue resulted in 102,734 matches. Two objects were matched to multiple AllWISE objects, and were discarded from the sample. Vega to AB conversion factors for WISE photometry are given in the WISE Explanatory Supplement (Cutri et al., 2013)

2.1.4 *Completeness of Photometry*

Objects which are faint in the SDSS i band-passes are more likely to have magnitudes which fall below the limiting magnitudes of the UKIDSS and WISE band-passes at longer wavelengths. For a given i magnitude, a quasar with a blue spectrum is more likely to be undetected at longer wavelengths than a quasar with a red spectrum. Therefore, as we allow fainter quasars in to our sample we will be biased towards objects with redder spectra. We impose an observed i magnitude lower limit of 19.1 mag, which is the magnitude limit of the main SDSS colour-selection algorithm. We verified that above this limit the DR7Q-matched sample is 95% complete in all band-passes with S/N > 5 (excluding WISE $W3$ and $W4$) and that this fraction is not changing rapidly with the brightness of the sample.
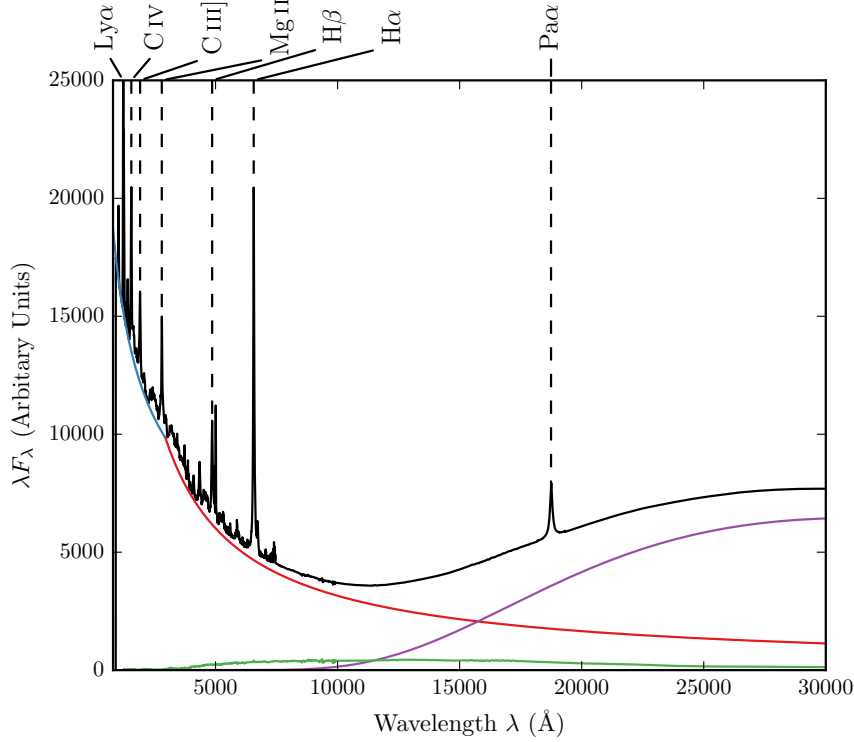
Figure 2.1: Model spectrum at $z = 1$, showing the contributions to the total flux from the blue power-law slope, red power-law slope, black-body and host galaxy. The locations of the most prominent emission lines in the spectrum are also indicated.

2.1.5 *Final Sample*

We exclude objects flagged as BALQSOs by Shen et al., (2011), since our model is unable to reproduce the broad absorption troughs that appear in the spectra of these objects. The final sample contains 61,411 objects in the redshift range $0.2 < z < 3.8$.

2.2 SED MODEL

I have constructed a new SED model which reproduces the SEDs of AGNs from the rest-frame UV ($\sim 0.1 \mu m$) to the rest-frame near-IR ($\sim 3 \mu m$). In this section, I will describe how I have modelled the emission from the various components contributing to the emission in this spectral region. The model spectrum is shown in Figure 2.1, with each of the main components indicated.

2.2.1 *Accretion Disk*

More than half the bolometric luminosity of an unobscured AGN is emitted in the Big Blue Bump, which extends from the near-IR at 1 µm to past 0.1 µm in the UV, and possibly all the way to the soft X-ray region. The Big Blue Bump emission is thought to arise from an accretion disc. In the 0.1 - 1 µm region the spectrum is generally characterised by a power-law of the form $F_\nu = C\nu^{-\alpha}$ where α is the power-law index, C is a constant, and F_ν is the flux per unit frequency, usually measured in units of erg s^{-1} cm^{-2} Hz^{-1}. Equivalently this can be expressed as $F_\lambda = C'\lambda^{\alpha-2}$ where F_λ is the flux per unit wavelength, usually measured in units of s^{-1} cm^{-2} Å^{-1}.

The value of the power-law index is uncertain. From a theoretical perspective, models of geometrically thin accretion discs (Shakura and Sunyaev, 1973) assume, in particular, that the disc is stationary, axisymmetric, and extends down to the innermost stable circular orbit, and that angular momentum is transported by local 'viscous' stresses that convert gravitational energy entirely into heat. This gives the dependence of the effective temperature on radius as $t_{eff} \propto r^{-3/4}$. A spectrum is then calculated by dividing the disc into concentric annuli, calculating the spectrum emitted by each annulus and then summing them all together. Assuming that each annulus radiates like a blackbody, the $r^{-3/4}$ effective temperature distribution gives $F_\nu \propto \nu^{1/3}$ (Peterson, 1997), although it is unclear whether this is consistent with observations.

In our model we characterised the Big Blue Bump from $\sim 0.1 - 1\mu$m as a broken power-law with three free parameters: a break-wavelength λ_{break}, a blue power-law index α_{blue} for wavelengths shorter than the break wavelength, and a red power-law index α_{red} for wavelengths longer than the break wavelength.

2.2.2 *Hot Dust*

At wavelengths longer than 1µm, emission from hot dust begins to dominate over emission from the accretion disc. The SED in this region is generally characterised either by a power-law ($\propto \lambda^{\beta_{NIR}}$), with $\beta \simeq 0.5$ (e.g. Richards et al., 2006a; Zhang et al., 2014), or by a blackbody at ~ 1300 K, thus peaking in the near-IR (e.g. Leipski et al., 2014). We modelled the hot dust emission using a simple blackbody:

$$F_\lambda = \frac{2hc^2}{\lambda^5} \frac{1}{e^{\frac{hc}{\lambda k_B T}} - 1} \tag{2.1}$$

The blackbody component has two free parameters: the temperature of the blackbody T_{BB} and the overall normalisation.

2.2.3 *Emission Lines*

Hundreds of emission lines are present in a typical AGN spectra. Some of the most prominent lines are shown in Figure 2.1. The emission line spectrum is taken from Maddox and Hewett, (2006), who extend the composite of Francis et al., (1991) to include the Hα (6560Å) and Paα (18750Å) emission lines. A single parameter, EL_{scale}, scales the equivalent widths of all emission lines equally:

$$F_\lambda = EL_{scale} \times \frac{F_{\lambda,el}}{F_{\lambda,cont}} \times F_\lambda \qquad (2.2)$$

where $F_{\lambda,el}$ is the line flux in the template, $F_{\lambda,cont}$ is the continuum flux in the template, and F_λ is the continuum flux in the model.

2.2.4 *Host Galaxy*

Emission from the host galaxy is important, particularly in the region around the 1μm inflection point in the quasar SED. While the host galaxies of bright quasars tend to be massive, bright ellipticals, the hosts of lower luminosity AGN can have disc components (e.g. Dunlop et al., 2003). Our model incorporates $z = 0$ Sa, Sb, Sc and elliptical-type templates from Mannucci et al., (2001), which for simplicity do not evolve with redshift. We characterise the relationship between the luminosity of the AGN L_{AGN} and the luminosity of the host galaxy L_{Gal} as a power-law

$$L_{Gal} = L_{AGN}^\beta \qquad (2.3)$$

with power-law index $\beta = 0.42$ (Maddox and Hewett, 2006). Dividing both sides of Equations 2.3 by the luminosity of the AGN gives the luminosity of the host galaxy relative to the luminosity of the AGN

$$\frac{L_{Gal}}{L_{AGN}} = L_{AGN}^{\beta-1} \qquad (2.4)$$

which for $\beta < 1$ decreases with increasing AGN luminosity. In a flux limited sample, the AGN luminosity will tend to increase with redshift and so the luminosity of the host galaxy relative to the luminosity of the quasar will decrease with increasing redshift. Hence, the contribution from the host galaxy to the total flux is important at low redshift, but becomes gradually less significant towards higher redshifts.

Since the contribution from the host galaxy to the flux changes as a function of AGN luminosity, and hence redshift, we choose a reference redshift z_{nrm} where we set the fractional contribution of the

host galaxy to the total flux, η. In an arbitrary region of the spectrum (we use $4000 - 5000$ Å) we calculate both the AGN continuum flux $F_{AGN}(z_{nrm})$ and the flux from our host galaxy template spectrum $F_{Gal}(z_{nrm})$. The fractional contribution from the host galaxy to the total flux is then:

$$\eta = \frac{CF_{Gal}(z_{nrm})}{F_{AGN}(z_{nrm}) + CF_{Gal}(z_{nrm})} \tag{2.5}$$

where the constant C is the factor by which we must multiply the unnormalised galaxy spectrum in order for Equation 2.5 to hold true. Rearranging for the constant C we find

$$C = \frac{\eta}{1-\eta} \frac{F_{AGN}(z_{nrm})}{F_{Gal}(z_{nrm})} \tag{2.6}$$

Hence at redshift z_{nrm} the host galaxy flux we add to our rest frame quasar continuum is

$$F_\lambda = \frac{\eta}{1-\eta} \frac{F_{AGN}(z_{nrm})}{F_{Gal}(z_{nrm})} F_{\lambda,Gal} \tag{2.7}$$

where $F_{\lambda,Gal}$ is our host galaxy template spectrum in the quasar rest frame. The contribution from the host galaxy at a different redshift z is given by

$$
\begin{aligned}
F_\lambda &= \frac{\eta}{1-\eta} \frac{F_{AGN}(z)}{F_{Gal}(z)} \frac{F_{AGN}(z_{nrm})}{F_{Gal}(z_{nrm})} \left(\frac{F_{AGN}(z)}{F_{Gal}(z)} \right)^{-1} F_{\lambda,Gal} & (2.8) \\
&= \frac{\eta}{1-\eta} \frac{F_{AGN}(z)}{F_{Gal}(z)} \frac{F_{AGN}(z_{nrm})}{F_{Gal}(z_{nrm})} \frac{F_{Gal}(z)}{F_{AGN}(z)} F_{\lambda,Gal} & (2.9) \\
&= \frac{\eta}{1-\eta} \frac{F_{AGN}(z)}{F_{Gal}(z)} \frac{L_{AGN}(z_{nrm})}{L_{Gal}(z_{nrm})} \frac{L_{Gal}(z)}{L_{AGN}(z)} F_{\lambda,Gal} & (2.10) \\
&= \frac{\eta}{1-\eta} \frac{F_{AGN}(z)}{F_{Gal}(z)} \frac{L_{AGN}(z_{nrm})}{L_{AGN}(z_{nrm})^\beta} \frac{L_{AGN}(z)^\beta}{L_{AGN}(z)} F_{\lambda,Gal} & (2.11) \\
&= \frac{\eta}{1-\eta} \frac{F_{AGN}(z)}{F_{Gal}(z)} \left(\frac{L_{AGN}(z)}{L_{AGN}(z_{nrm})} \right)^{\beta-1} F_{\lambda,Gal} & (2.12)
\end{aligned}
$$

We need to know how the luminosity of the AGN depends on redshift. This is given by:

$$\frac{L_{AGN}(z)}{L_{AGN}(z_{nrm})} = 10^{-0.4(M_{AGN}(z) - M_{AGN}(z_{nrm}))} \tag{2.13}$$

where $M_{AGN}(z)$, the absolute magnitude of an AGN at redshift z, is given by

$$M(z) = m - 5(\log_{10} D_L(z) - 1) \qquad (2.14)$$

and $D_L(z)$ is the luminosity distance to a source at redshift z in parsecs. Hence:

$$\frac{L_{AGN}(z)}{L_{AGN}(z_{nrm})} = 10^{-0.4(M_{AGN}(z) - M_{AGN}(z_{nrm}))} \qquad (2.15)$$

$$= 10^{\left(\log_{10}\left(\frac{D_L(z)}{D_L(z_{nrm})}\right)^2\right)} \qquad (2.16)$$

2.2.5 *Lyman-α Forest Absorption*

The optical spectra of high redshift quasars show hundreds of sharp absorption lines, which mostly correspond to the redshifted neutral hydrogen Lyα 1216Å transition. These absorption features are collectively referred to as the *Lyman-α forest*. To simulate the effect of Lyman-α forest absorption on our model SED we use the parametrisation of Becker et al., (2013), who derived an analytic function for the effective optical depth τ_{eff} over the redshift range $2 < z < 5$ made using 6065 quasar spectra from SDSS DR7. In their model the effective optical depth τ_{eff} is given by

$$\tau_{eff} = \tau_0 \times \left(\left(\frac{1+z}{1+z_0}\right)^b + C\right) \qquad (2.17)$$

where,

$$
\begin{aligned}
t_0 &= 0.751 \\
b &= 2.9 \\
C &= -0.132 \\
z_0 &= 3.5
\end{aligned}
$$

The transmitted flux $F_{\lambda,trans}$ at redshift z is then given by

$$f_{\lambda,trans} = F_\lambda \times e^{-\tau_{eff}} \qquad (2.18)$$

An absorption line at λ_{abs} in the rest-frame of an AGN at redshift z_{AGN} has wavelength

$$(1 + z_{AGN})\lambda_{abs} \qquad (2.19)$$

in the rest frame of an observer on Earth. In the rest-frame of a cloud of neutral hydrogen at redshift z_{cloud} the absorption line has wavelength

$$\frac{(1 + z_{\text{AGN}})\lambda_{\text{abs}}}{(1 + z_{\text{cloud}})} \tag{2.20}$$

and so to absorb Lyman-α at 1216 Å the gas cloud must be at a redshift

$$z_{\text{cloud}} = \frac{(1 + z_{\text{AGN}})\lambda_{\text{abs}}}{1216\text{Å}} - 1 \tag{2.21}$$

For every wavelength $\lambda_{\text{abs}} < 1216$ Å in the rest-frame of an AGN at redshift $z > 2$ we calculate z_{cloud} using Equation 2.21 and then calculate the transmitted flux at λ_{abs} by substituting z_{cloud} in to Equations 2.17 and 2.18.

2.2.6 *Lyman-Limit Systems*

Lyman-limit systems are clouds of HI which are optically thick at the Lyman limit (912Å), which generally implies a neutral hydrogen column density $N(\text{HI}) > 10^{17}\text{cm}^{-2}$. Photons at wavelengths shorter than the Lyman-limit will be absorbed, which creates a sharp break in the observed continuum. We model the effect of a Lyman-limit system at the redshift of the quasar by setting the flux at wavelengths less that 912Å in the quasar rest frame to zero.

2.2.7 *Dust Extinction*

The selection criteria of the SDSS DR7Q catalogue, and particularly the DR10Q catalogue, are sensitive to quasars with moderate amounts of dust reddening (possibly as high as E(B-V) ~ 0.5; Richards et al., 2003) at the redshift of the quasar, and so we included the effect of dust extinction in our model. We considered four types of extinction curve: the Large Magellanic Cloud (LMC), Small Magellanic Cloud (SMC), Milky-Way (MW) extinction curves from Pei, (1992) and an extinction curve appropriate for the quasar population which has been derived by Paul Hewett. To derive the quasar extinction curve, UKIDSS photometry was used to provide an E(B-V) estimate, via the magnitude displacement of each quasar from the locus of unreddened objects. At redshifts $2 < z < 3$ the reddening measure is made at rest-frame wavelengths 3500-7000Å, where Galaxy, LMC and SMC extinction curves are very similar. The SDSS spectra of the same objects are then employed to generate an empirical extinction curve in the ultraviolet, down to 1200Å. The resulting curve has no 2200Å feature and rises rapidly with decreasing wavelength but is not as steep as the SMC curve. The extinctions curves give the colour excess $E(B - \lambda)$ relative to the colour excess $E(B - V)$ as a function of

wavelength λ. The colour excess $E(B-V)$ is related to the extinction in the V band, $A(V)$, via a parameter R,

$$A(V) = R \times E(B-V) \tag{2.22}$$

where $R = 3.1$ in the MW and $R \simeq 3$ in the Magellanic Clouds. Hence the extinction at a wavelength lambda $A(\lambda)$ is

$$A(\lambda) = E(B-V) \times \left[\frac{E(\lambda-V)}{E(B-V)} + R \right] \tag{2.23}$$

where the colour excess $E(B-V)$ is a free parameter in our model. The attenuation of the flux at a given wavelength is then:

$$F_\lambda = F_\lambda 10^{-A(\lambda)/2.5} \tag{2.24}$$

in the rest frame of the quasar.

2.3 THE 'STANDARD' SED MODEL

We will begin by deriving a 'standard' SED model by constraining a single set of parameters with a large sample of $0.2 < z < 4$ quasars encompassing a range of luminosities, accretion rates etc. The free parameters in our model are the blue power-law slope, the red power-law slope, the power-law break wavelength, the blackbody temperature, the blackbody normalisation, the emission line equivalent width scaling, and the fractional contribution from the host galaxy to the total flux. The reddening E(B-V) is fixed to zero, since a large fraction of SDSS quasars have very small amounts of dust reddening (Richards et al., 2003). For the host galaxy we use a Sb-type template derived by Mannucci et al., (2001). With some choice of initial parameters, we generate a set of model observed spectra at redshifts from $z = 0.25$ to $z = 3.75$ in intervals of $\Delta z = 0.1$. We then transform our set of model spectra into a set of model $ugrizYJHKW1W2$ SEDs

The throughput functions of the SDSS $ugriz$, UKIDSS YJHK and WISE $W1W2W3$ band-passes are shown in Figure 2.2, along with our model AGN spectra at three different redshifts. The mean flux density in a band-pass P is given by

$$f_\lambda(P) = \frac{\int P(\lambda) f_\lambda(\lambda) \lambda d\lambda}{\int P(\lambda) \lambda d\lambda} \tag{2.25}$$

where $P(\lambda)$ is the dimensionless throughput function of the band-pass. The corresponding magnitude, $m_\lambda(P)$, is then

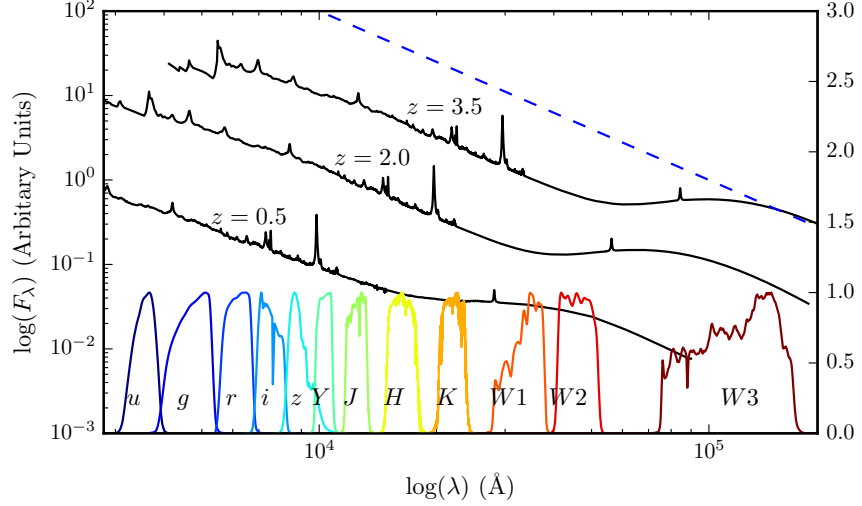$$m_\lambda(P) = -2.5 \log(f_\lambda(P)) - m_0(P) \tag{2.26}$$

Figure 2.2: Model spectrum at three different redshifts (each arbitrarily scaled), and throughput functions for SDSS, UKIDSS and WISE band-passes (scaled so that the peak transmission is equal to one.) The dashed line indicates the slope of the AB magnitude system zero point.

where $m_0(P)$ is the zero-point magnitude of band P. In the AB magnitude system, the zero-point flux per unit wavelength is

$$\frac{f_\lambda(\lambda)}{\mathrm{erg\ cm^{-2}\ s^{-1} \mathring{A}^{-1}}} = 0.1087 \left(\frac{\lambda}{\mathring{A}}\right)^{-2}. \qquad (2.27)$$

This is substituted into Equation 2.25 to give a zero-point mean flux density which is then converted into a corresponding magnitude.

The model SEDs are normalised such that the i magnitude of each model SED is 18.0 mag. This gives us an array of model magnitudes as a function of redshift and band-pass. We generate an equivalent data array by dividing our quasar sample into redshift bins from $z = 0.2$ to $z = 3.8$ with bin width $\Delta z = 0.1$. We normalise the individual quasar SEDs such that the observed i magnitude is equal to 18.0 mag, and then calculate a median SED in each redshift bin.

To fit the model to the data we minimise the sum of the squares of the differences between the elements in the model magnitude array and the elements in the data magnitude array. The minimisation is done using the 'nelder-mead' algorithm. Our SED model is valid only up to $\lambda \sim 3\mu m$ in the quasar rest frame (the approximate wavelength of the peak in hot dust emission); beyond this additional contributions to the total flux from cooler dust will become significant. This prevents us from using the two highest wavelength WISE bands in the fit. We also exclude the SDSS u and g band-passes from the fit at $z > 2.7$ and $z > 3.7$ respectively, where absorption in the Lymanα forest becomes large.

Parameter	Symbol	Before Correction	After Correction
Blue power-law index	α_{blue}	0.58	0.58
Red power-law index	α_{red}	-0.04	-0.05
Power-law break	λ_{break}	2945	2957
Blackbody temperature	T_{BB}	1216 K	1186 K
Blackbody normalisation	C_{BB}	0.22	0.21
Emission line scaling	C_{EL}	0.63	0.73
Galaxy fraction	η	0.29	0.28
E(B-V)	E(B-V)	0.00	0.00

Table 2.1: Best-fitting parameters from fit to DR7Q-matched sample. Only give best-fit values after correction.

The best-fitting parameters from the fit are shown in Table 2.1. The *Re-do fit* colours ($u - g$, $g - r$, etc.) of the median SED, the individual quasars, and the best-fitting model are plotted as a function of redshift in Figs. 2.3 and 2.4. Most of the large variations that can be seen in the median colours of the quasars as a function of redshift are due to strong emission lines being redshifted in to and out of the bandpasses of the band-passes being used.

2.4 DISCUSSION OF FIT

In Figure 2.5 we show the difference between the magnitudes from the best-fitting model and the median magnitudes from the sample. We have transformed the effective wavelengths of the band-passes to the rest frame of the quasars in each redshift bin, to give to the residuals as a function of rest-frame wavelength. We represent the residuals measured in each band-pass using a different coloured line. Differences between residuals from different band-passes at the same rest-frame wavelength could indicate redshift evolution of the typical quasar SED.

The residuals indicate that over a large redshift range the model does a fairly good at reproducing the median observed colours of the DR7Q-matched sample. Most discrepancies are at the < 0.1 mag level. It is remarkable that a single model is so effective; the properties of a typical quasar to not change significantly over a wide range of red-shifts and luminosities. On the other hand, for the individual objects there is a significant scatter about the mean. In general, our goal is to use this intrinsic spread in SED properties in order to understand the diversity in physical quasar properties.
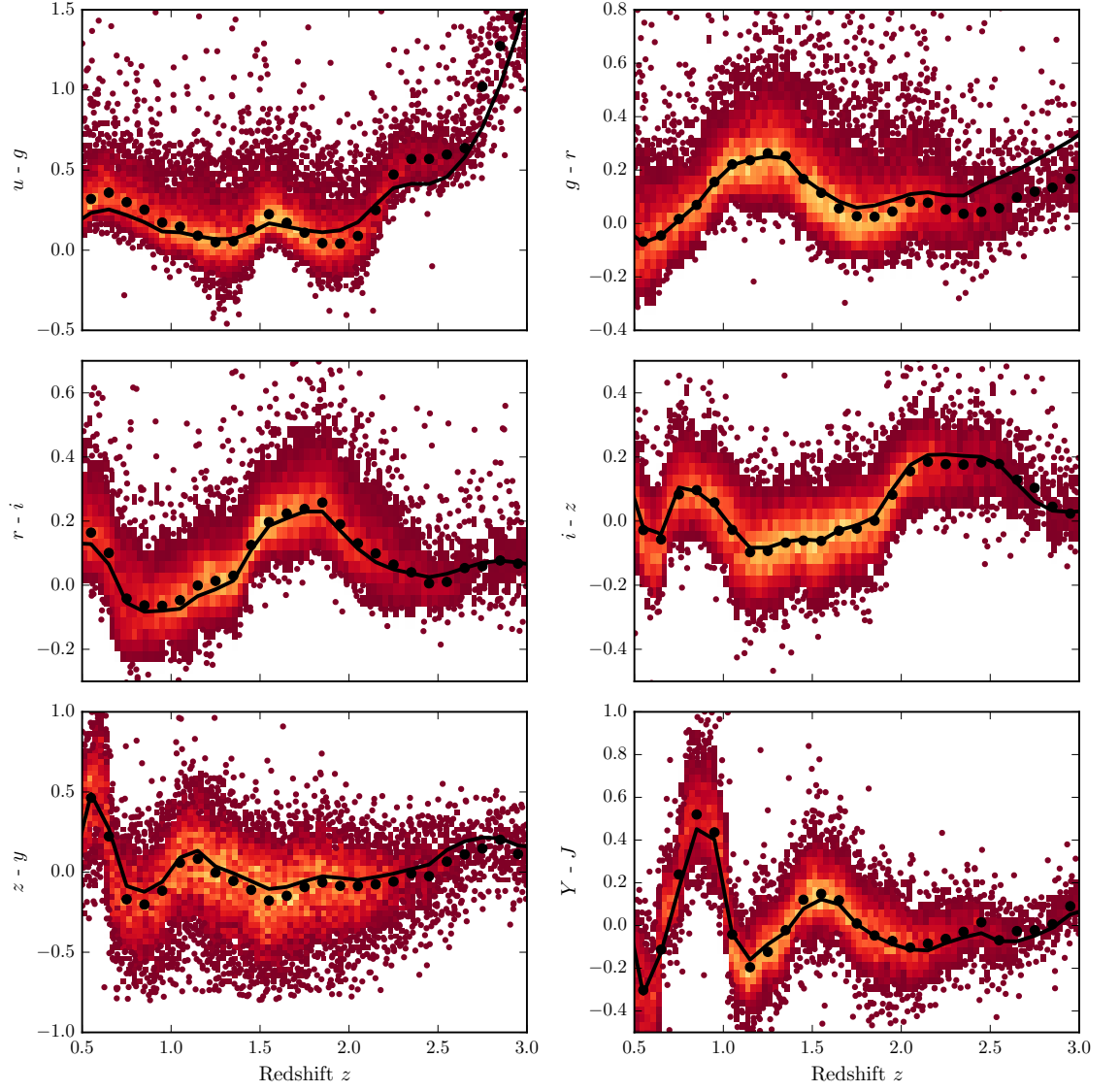
Figure 2.3: Colours of median SED (*black circles*), individual objects (*grey points*), best-fitting model (*black line*) as a function of redshift.
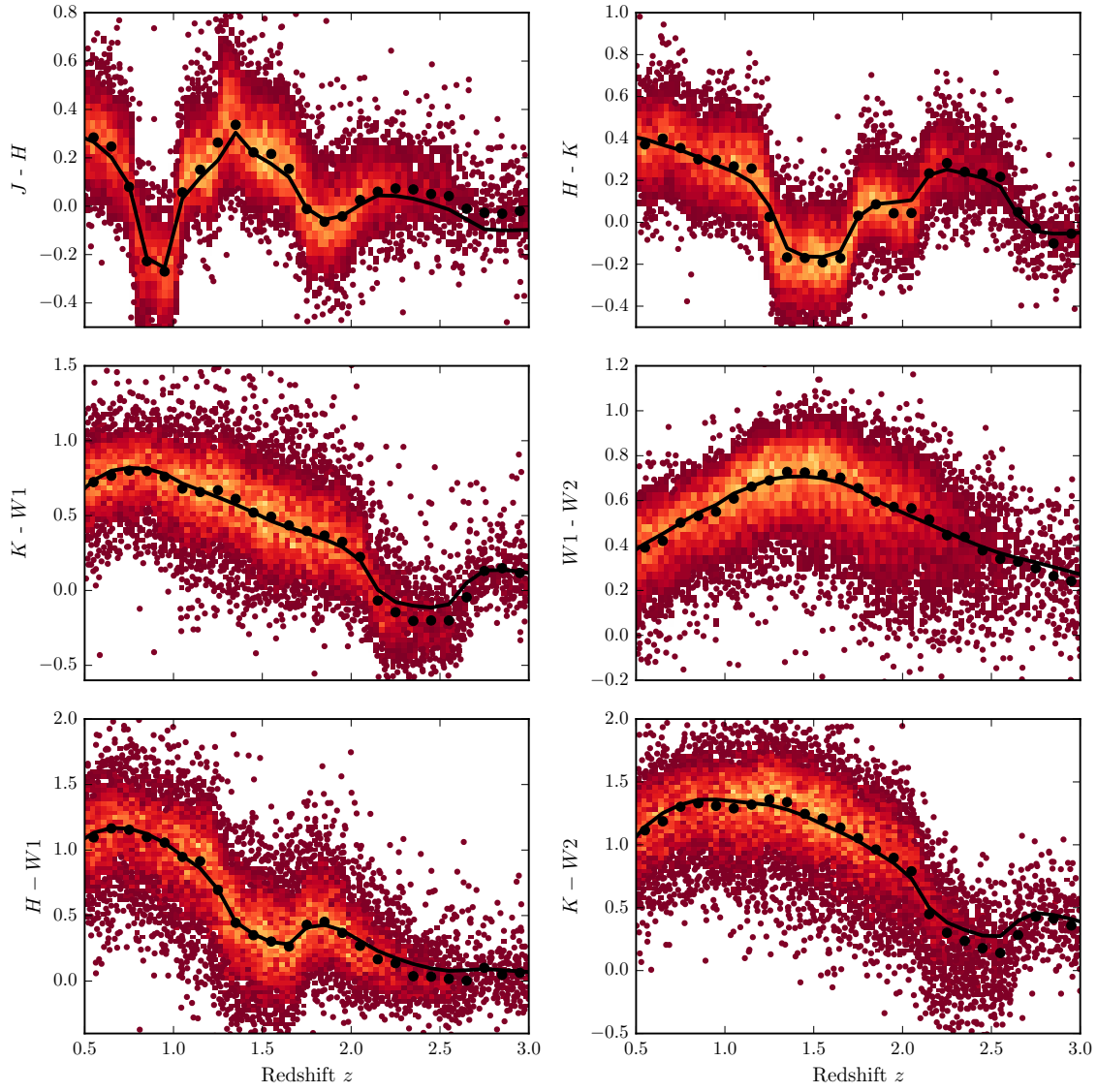
Figure 2.4: Colours of median SED (*black circles*), individual objects (*grey points*), best-fitting model (*black line*) as a function of redshift.
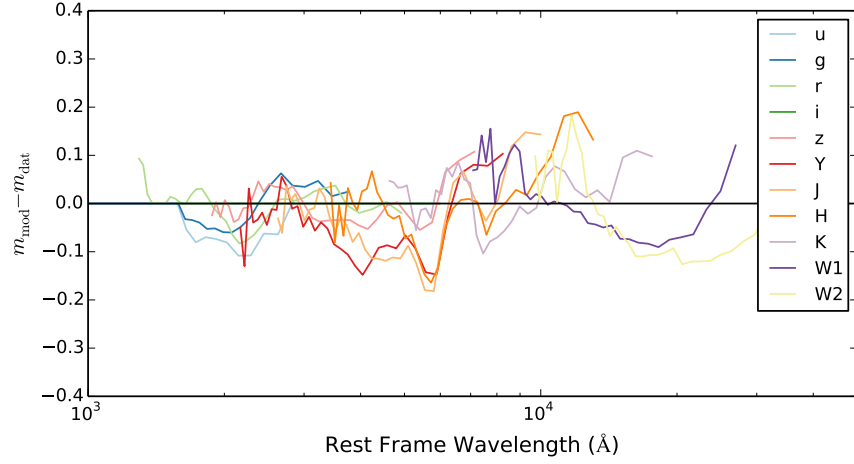
Figure 2.5: Residuals from fit to DR7Q-matched catalogue as a function of rest-frame wavelength.

2.4.1 *Flux Correction*

2.5 HOT DUST

Including a black-body with T~1250K, a simple parametric model matches the ugrizYJHKW1W2 (SDSS+UKIDSS+WISE) median colours of luminous quasars at redshifts $0.2 < z < 0.4$ extraordinarily well. The spread in the KW1W2 colours (Figure 2.8), probing the rest-frame ~1-2 micron region, is significant and strongly suggests presence of real variation in the "hot dust" temperature and luminosity among the quasars. Several other investigations have drawn attention to the rest-frame near-infrared SEDs, with populations of 'dust free' objects postulated (Hao et al., 2010; Hao et al., 2011; Jiang et al., 2010; Mor and Trakhtenbrot, 2011)

Reverberation measurements of nearby AGNs suggest that hot dust very close to the central source (few tens of light days; e.g. Minezaki et al., 2004; Suganuma et al., 2006). The hot dust signature could contain information about inner face of an obscuring torus structure and/or constrain the dust content of an accretion disk wind. Several studies have shown that the luminosity of the NIR excess emission correlates with that of the central engine with a slope close to unity e.g. Gallagher et al., 2007, suggesting that the dust is reprocessing radiation from the accretion disc.

Outflows may emerge from the outer region of the accretion disc or even the innermost region of the torus, in which the gas clouds are dusty and relatively cold. Indeed, there is observational evidence for dusty outflows close to the central engine (e.g. Bowler et al., 2014). The dust is heated by the central engine, and radiates in the near-infrared band. Wang et al., (2013), fitting the NIR emission with a

single power-law, found that objects with strong outflow signatures (blue-shifted C IV) have more hot dust emission relative to the accretion disc emission in a large sample of $z \sim 2$ non-BAL quasars. It could be that this correlation is induced by a third factor that simultaneously affects outflows and dust emission, for instance the inclination angle or metallicity. Alternatively the dust could be intrinsic to outflows and may have a non-trivial contribution to the outflow acceleration.

2.5.1 *Parameterising the hot dust emission*

We characterise the hot dust properties of our sample in terms of the temperature and luminosity of a blackbody. We choose to parameterise the luminosity in terms of the NIR to UV luminosity ratio (which is proportional to the covering factor of hot dust (L_{NIR}/L_{Bol}) used in other studies (Roseboom et al., 2013). The UV and NIR luminosity are calculated between 2000 and 9000Åand 1 and 3 µm respectively.

In Figure 2.6 we see that the two parameters are clearly correlated. For a lower temperature black-body the NIR to UV luminosity ratio is larger. Such a correlation is to be expected: as the black-body temperature is lowered, the peak shifts to longer-wavelengths (following Wien's displacement law). Because of this degeneracy we need to be very careful to seperate out real trends of $R_{NIR/UV}$ with other quasar properties from indirect trends resulting from a mutual dependence on T_{BB}.

Some previous studies (e.g. Wang et al., 2013; Zhang et al., 2014) have instead paramterised the near-IR emission using a power-law. We tested this parameterisation, and evaluated it's effectiveness relative to using a black-body. The power-law is normalised at 9000A, where its flux is set equal to the flux of the UV/optical model. The NIR power-law slope is fit between ~1 and 2.4µm (with the exact wavelength region being fit depending on the redshift of the quasar). We found large residuals in the best-fitting model which varied systematically as a function of $\lambda_{eff}/(1+z)$. This suggests that the power-law model is a poor fit to the shape of the near-IR emission. One needs to take care in looking at trends with luminosity given the observed-frame passband information on the rest-frame SED can produce some strong systematics with redshift, particularly if the SED-model is not a good fit to the actual SED. A similar conclusion was reached by Gallagher et al.

2.5.2 *Sample*

Our goal is to determine the temperature and abundance of the hot dust component in individual quasars. These properties will be mea-
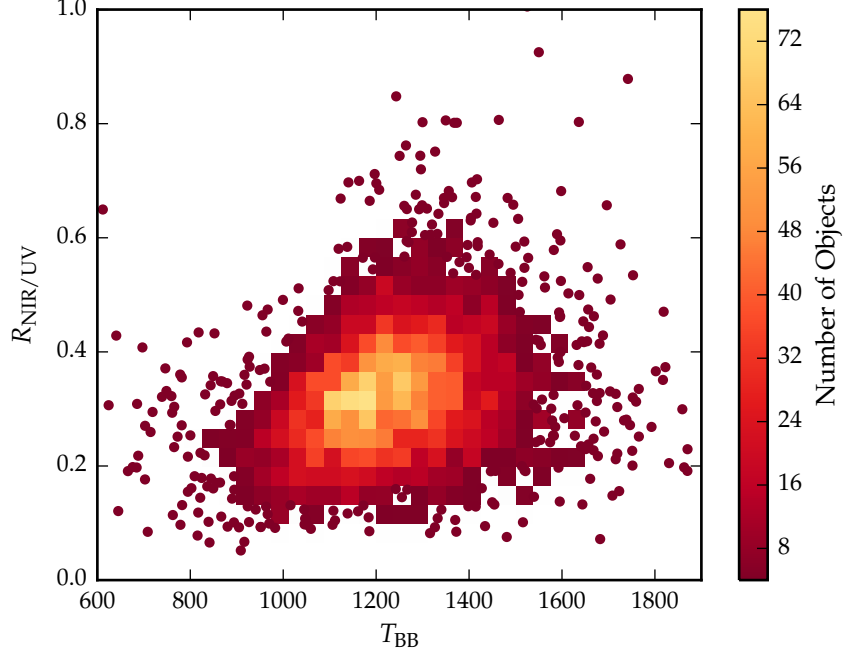
Figure 2.6: Ratio of NIR to UV luminosity ($R_{\mathrm{NIR/UV}}$) against temperature (T_{BB}) for low-z sample. The density of points is shown in more dense regions of the space, and individual objects in less dense regions.

sured by fitting a model to the SDSS-UKIDSS-WISE photometry. Constraing a T~1200K blackbody component in the SED model requires photometric data covering ~1-3μm in the rest-frame of the quasar.

The observed-frame wavelength coverage of the available passbands limits the redshift range of the quasars which can be used. One does need to take care in looking at trends with luminosity given the observed-frame passband information on the rest-frame SED can produce some strong systematics with redshift, particularly if the SED-model is not a good fit to the actual SED. We consider only quasars at redshifts $z > 1$ where the relative host galaxy contribution to the SED is negligible. At redshifts $1 \lesssim z \lesssim 1.5$ the available ugrizYJHKW1W2 photometry provides good coverage of the rest-frame SED up to ~2μm. At $z \sim 1.5$ the W2 passband is shifted to ~1.8μm; at higher redshifts the wavelength coverage of the W2 band becomes much less than the peak wavelength of a T~1200K blackbody and experiments showed that such a component can not be adequately constrained by the available photometry. Quasars in the redshift interval $1.5 < z < 2$ are therefore excluded from our sample.

For the quasars at $z \sim 1$ the WISE W3 band is probing rest-frame wavelengths of $\sim 5 - 6$μm. This region of the SED is dominated by emission from cooler, more distant dust, which is not accounted for in our model. However, at redshifts $z \gtrsim 2$ the WISE W3 passband probes

sufficiently short wavelengths to be useful in constraining the shape of the hot blackbody component. Therefore for quasars at redshifts $z > 2$ we again have sufficient constraints from the ugrizYJHKW1W2W3 photometry to determine the temperature and normalisation of the blackbody component. There are few objects in our sample with redshifts $z > 2.7$, and so we set this as an upper limit on the redshift of our sample. Because of these constraints, our sample is divided in to two parts: one at low redshifts ($1 < z < 1.5$) and the other at higher redshifts ($2 < z < 2.7$).

We include only quasars with observed magnitudes brighter than 19.1 in the i band-pass, i.e. the quasars selected by the main SDSS quasar selection algorithm (70,214 quasars). Cross-matching (with a 2″ radius and picking only the nearest neighbour) the SDSS DR7Q catalogue with the ULAS catalogue, which covers only ∼ 38% of the SDSS foot-print, resulted in 37,886 matches. Of these 36,628 have been detected in one or more of the WISE band-passes. We exclude quasars flagged as broad-absorption line quasars from the sample (leaving 35,272 quasars). We impose a lower-limit signal-to-noise ratio (S/N) > 5 magnitudes in the K, $W1$ and $W2$ band-passes for the low-z sample and S/N > 5 in the $W1$, $W2$, and $W3$ band-passes for the high-z sample to ensure reliable photometry. This gives us 5,910 quasars in our low-z sample and 1,989 quasars in our high-z sample.

We will hold most parameters fixed, and vary only those we are interested in, i.e. the blackbody parameters which parameterise the NIR emission. Therefore we need to define a sub-sample of objects which we know are well fit by our standard SED model in the UV/optical region. This means excluding objects with extreme emission line equivalent widths or significant dust extinction. We use the $i - K$ colours of the quasars as a measure of the overall colour of the quasars as it provides the longest baseline in wavelength without being affected by absorption in the Lyα forest at high redshifts. We discarded from our sample quasars with $i - K$ colors redder than our standard model with dust reddening E(B-V) = 0.075 and bluer than E(B-V) = -0.075 (Figure 2.7). Following this cut we are left with 4,615 quasars in our low-z sample and 1,692 quasars in our high-z sample.

2.5.3 *Diversity in hot dust properties*

In Figure 2.8 we plot the $W1 - W2$ colors of the DR7Q-matched sample as a function of redshift at z < 3. In this redshift range the $W1$ and $W2$ band-passes are probing the 1.2 - 2.8μm and 1.6 - 3.8 μ region of the rest frame SED respectively. For reference, the peak wavelength is at 2.4μm for a black-body radiating at 1200K (close to the sublimation temperature of dust grains). At any given redshift we see a ∼ 0.5 mag dispersion in the $W1 - W2$ colors.
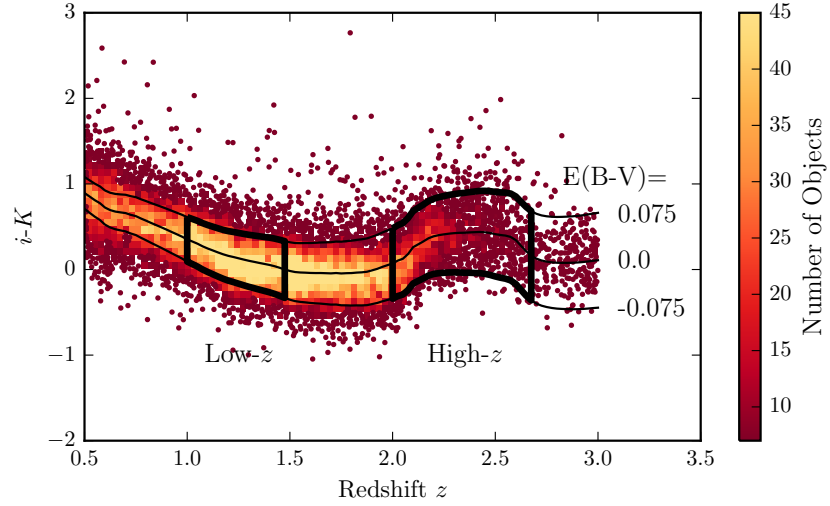
Figure 2.7: i − K vs z. Demonstrates how sample was defined. The grey points show, as a function of redshift, the i − K colours of all DR7Q quasars which are not classified as broad-absorption line quasars by Shen et al. and i magnitude > 19.1. The black line shows the i − K colour of our standard, unreddened SED model as a function of redshift. The red and blue lines show the i − K colours of our SED model with dust reddening E(B-V) = 0.075 and E(B-V) = -0.075 respectively. A significant amount of this reddening can be attributed to intrinsics variations in the UV power-law slopes of the indidual quasars, which is why we allow a negative reddening. However, there is a clear 'red tail' to the colour distribution which can be explained by dust reddending at the redshift of the quasar. We definined two samples, at low (0.5 < z < 1.5) and high (2 < z < 2.7) redshift, which are shown in the figure.
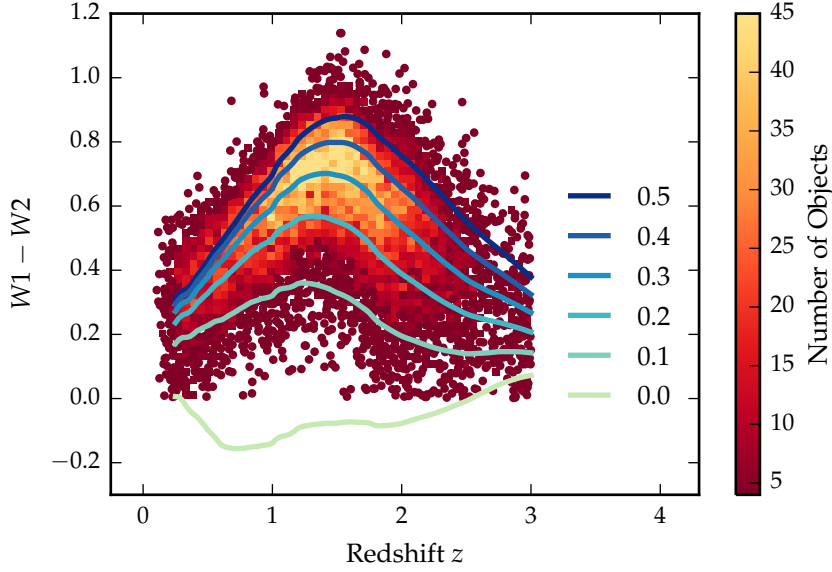
Figure 2.8: $W1 - W2$ colours of DR7 sample as a function of redshift. Above a certain density threshold points are represented by a density plot. On top we plot the colours of our standard SED model, with a fixed temperature and a varying NIR (1 - 3 μm) to UV ratio.

On the same axes in the Figure we have plotted the $W1 - W2$ colors derived from our SED model with a fixed blackbody temperature (1216K) and a ratio of NIR to UV luminosity ranging from 0.0 to 1.0, with the other model parameters held constant. We conclude that even with the sample restricted to be fairly uniform in its UV/optical properties, we still get an interesting spread in W1-W2 colors, which we can use to learn about the diversity of NIR properties in our sample. In the rest of this chapter we will characterise the hot dust properties of our sample, and test its relation to quasar properties such as luminosity, black-hole mass and normalised accretion rate, and outflow-properties.

In Figure 2.6 we show that there is quite a range of temperature and normalisation present in our sample. However, we need to check how much of this is due simply to uncertainties in the fits stemming from uncertainties in the photometry. In order to achieve this we took our standard SED model with a single temperature and normalisation black-body component, and generated 200 mock SEDs with a brightness distribution similar to that of our real sample. We estimated the mean uncertainty of the magnitudes in the K, W1, and W2 band-passes as a function of apparent brightness. We then sampled the K, W1, and W2 magnitudes from Gaussian distributions, with a mean equal to the magnitude of the model SED, and the width equal to the mean uncertainty at the appropriate brightness. Finally,
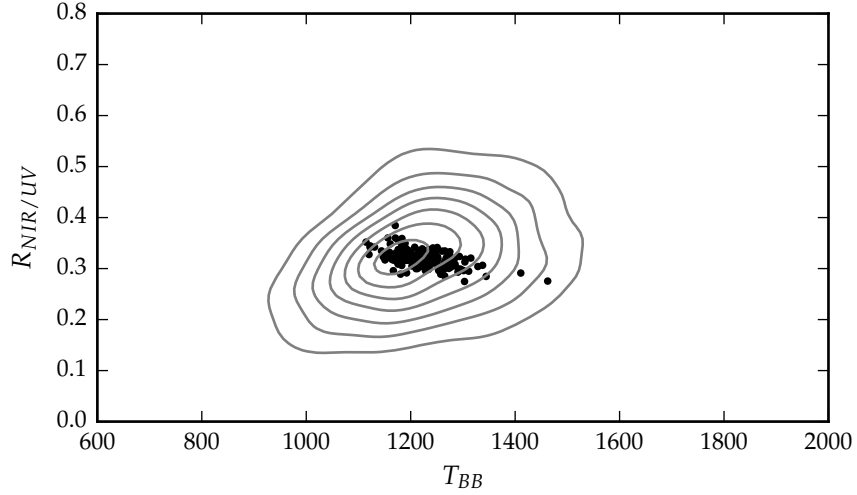
Figure 2.9: Ratio of NIR to UV luminosity ($R_{NIR/UV}$) against temperature (T_{BB}). The grey contours show equally-spaced lines of constant probability density generated using a Gaussian kernal-density estimator on our data sample. The black points are for our mock data.

we fit these mock SEDs using our standard fitting procedure. The results are shown in the Figure below, on top of the results from our real sample (shown as grey contours). We can see that uncertainty in the photometry introduces a significant scatter to the temperature, but that this scatter is less than the intrinsic scatter in the data. This demonstrates that there is a real distribution of hot dust temperatures and luminosities in our sample.

2.6 FITTING PROCEDURE

We will fit a model to the individual quasar SEDs, allowing the temperature and normalisation of the black body component to vary. The model spectrum is redshifted to the redshift of the quasar being fit and is then multiplied by the $ugrizYJHMW1W2W3$ throughput functions and normalised appropriately to give AB magnitudes. To fit the model to the data we minimise the sum of the squares of the differences between the elements in the model magnitude array and the elements in the data magnitude array. To avoid significant absorption in the Lyman-α forest at high-z, we restrict our fitting to wavelengths greater than 2000A; when the effective wavelength of a band-pass falls below this limit the band-pass is excluded from the fit. The minimisation is done using the 'nelder-mead' method, as implemented in the `minimize` function from the Python module `scipy`.

2000A is quite large given the Lyman-alpha forest impacts from 1216A.
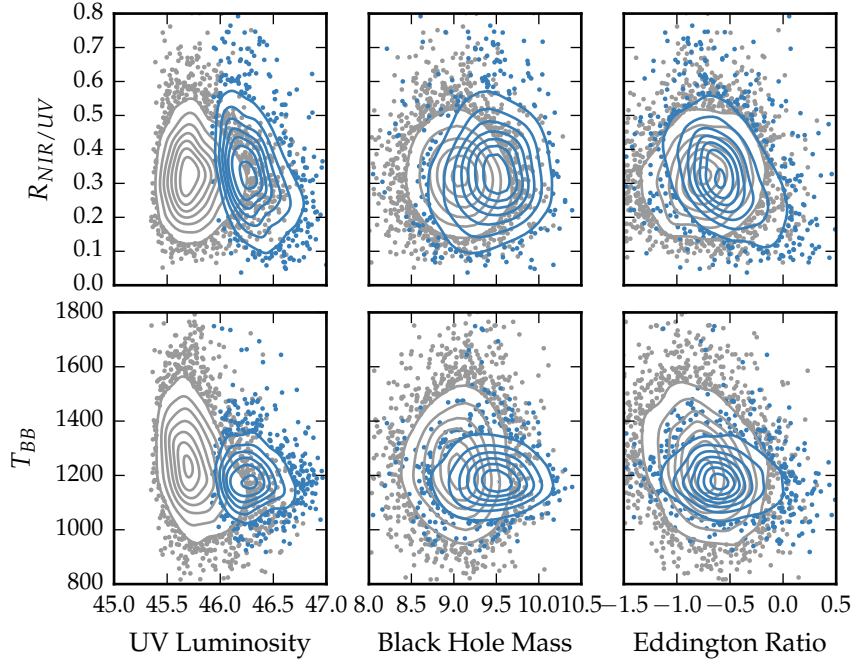
32

Figure 2.10: Best-fit black-body temperature against UV luminosity (left), black-hole mass (center) and Eddington ratio (right) for $1 < z < 1.5$ sample (black) and $2 < z < 2.7$ sample (black). In region of high-density we represent the density with contours generated using a Gaussian kernel density estimation. Needs re-making with new BH masses.

2.7 RESULTS

2.7.1 *Correlations with quasar properties*

We now look for correlations between the properties of the black-bodies we have fitted to the hot dust emission and other properties of the quasar such as redshift, black-hole mass, and normalised accretion rate (Eddington ratio).

Calculate new BH masses and redo this sectin.

2.7.2 *Spectral properties*

In the dusty wind model - first proposed by Konigl and Kartje, (1994) and later developed by, amongst others, Everett, (2005), Elitzur and Shlosman, (2006), Keating et al., (2012) - the 'torus' is the dusty part of a magneto-hydrodynamic wind beyond the dust sublimation radius. The MHD wind is roughly polar, and so the hot dust forms a vertical 'wall' around the accretion disk. UV photons from the accretion disk accelerate the wind via radiation line driving. That flattens the geometry of the wind and exposes more surface area that is viewable on a relatively face-on line of sight. The radiation pressure is increased

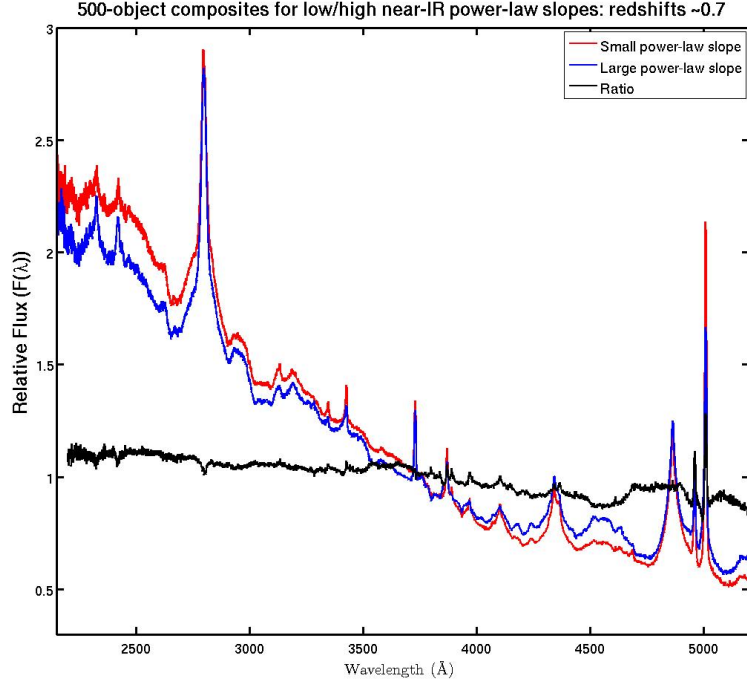**500-object composites for low/high near-IR power-law slopes: redshifts ~0.7**

Figure 2.11: Composite SDSS spectra for objects at z ~ 0.7. We have divided sample into objects with objects best-fit by small (red line) and large (red line) values of β. Change this to select by $R_{NIR/UV}$ / T_{BB}. Label prominent emission lines.

at higher luminosities and/or accretion rates. This can flatten the geometry of the wind, thereby increasing the range of angles for which the inner edge of the dusty wind - where dust is at it's sublimation temperature - can be observed. A direct prediction is therefore that the in a quasars with high accretion rates and strong outflows, the emission from hot dust should be enhanced.

Low-z

The z < 0.8 SDSS spectrum composite comparison for the small and large β_{NIR} sub-samples is a very direct illustration of the Boroson and Green, (1992) Eigenvector 1 describing the spectral variation in the optical spectra of quasars; as Fe II EW increases the [O III] EW decreases. Hot dust emission increases with Fe II EW (Shen and Ho, 2014). We also note that the amount of hot dust correlates with the Si III/C III] emission ratios. The Si III/C III] ratio is generally considered to be a good indicator of density and is one of the primary EV1 correlates. The relative flux ratio of Si III to C III] increases when C IV is more blue-shifted (Richards et al., 2011). The Mg II emission line has exactly the same profile/shape for the two samples (apparent changes in Mg II seen in Fig. 2.11 are the result of changes in Fe II at
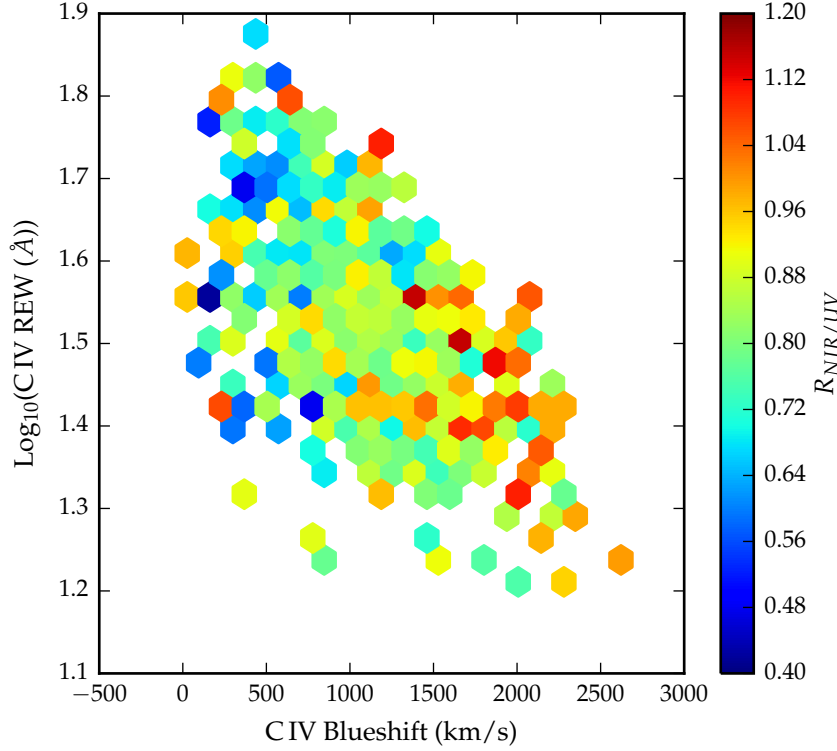
Figure 2.12: Rest-frame equivalent width and blueshift of the C IV line for 7,115 SDSS DR7 quasars. The colours of the hexagons denote the median hot dust (T≃1200 K) abundance for all quasars at a given equivalent width and blueshift. Quasars with the most extreme outflow signatures are predominantly hot-dust rich. Only bins containing a minimum of two objects are plotted.

wavelengths just shortward of the line). Finally, we note that objects with more hot dust are slightly redder.

High-z

In Fig. 2.12 we show how the ratio of NIR to UV luminosity depends on the blueshift and rest-frame equivalent width of the C IV line. C IV blueshifts are calclulated as in Section XX. We see that the NIR to UV luminosity ratio is strongly correlated with the blue-shift of the C IV emission line. A similar trend was noted by Wang et al., (2013). Interestingly, we note strong similarities to the object subsets selected according to their C IV-emission properties in Richards et al., (2011) (see Figures 11 & 12). We note that the correlation between the hot dust and the C IV emission properties will lead to apparent correlations between the host dust and the BH mass.

Need to re-do this and understand why beta-related trend is apparently stronger than with the blackbody parameters.
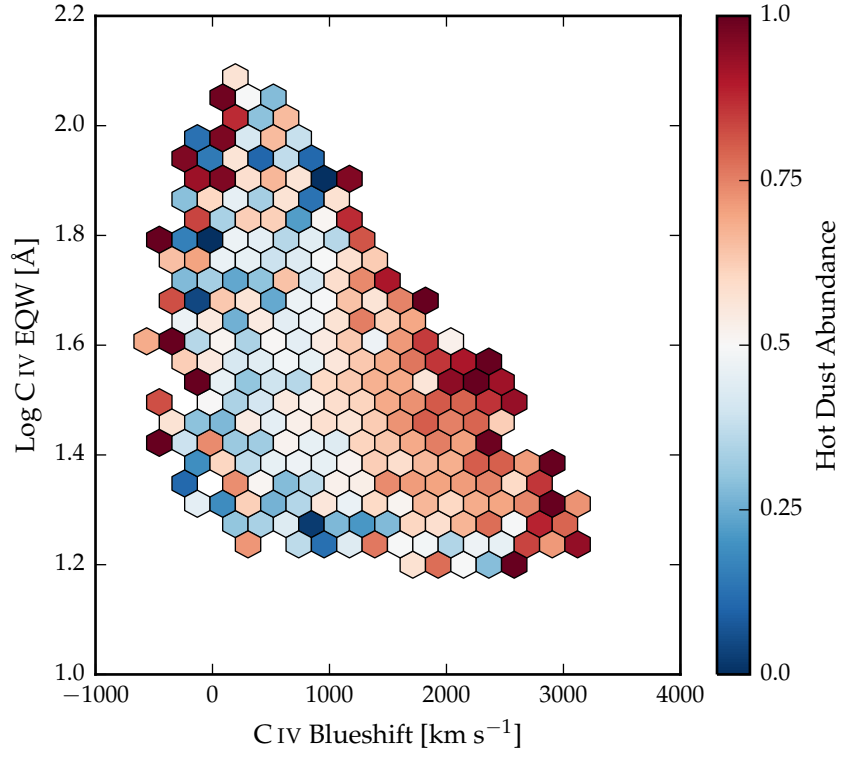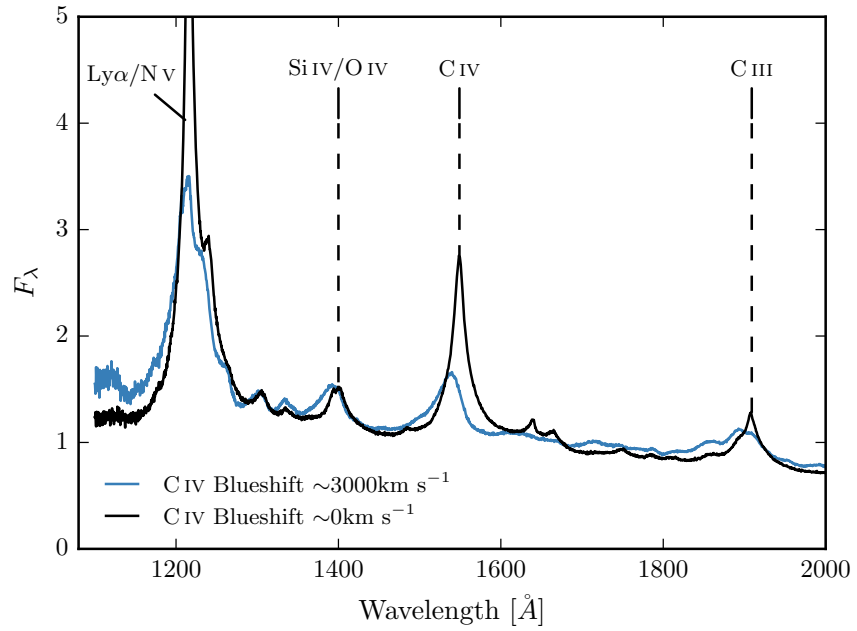
Figure 2.13

Figure 2.14

2.7.3 *BALs and radio-loud/radio-quiet*

In the spectra of about 20% of all quasars we observe broad (> 2000km/s) blue-shifted absorption troughs which are associated with quasar-driven out-flowing gas. BAL quasars in general have redder UV continua than non-BAL quasars, which is interpreted as the result of dust extinction. BAL quasars, on average, also have higher Eddington ratios and luminosities than non-BAL quasars.

We defined a sample of BAL quasars using the same method we used to define our sample of non-BAL quasars. At $1 < z < 1.5$ there are very few BAL quasars in our sample. In the $2 < z < 2.7$ redshift region we have 394 HiBAL quasars (the wavelength coverage of the SDSS spectra are not sensitive to LoBALs at these redshifts). Since BAL quasars are expected to suffer more from extinction due to dust, we have allowed E(B-V) to vary for the BAL quasar sample.

We find that the black-body temperature distributions are consistent (median T_{BB} for both samples = 1180K), but the ratio of NIR to UV emission is higher in BALs ($R_{NIR/UV}$ = 0.92 and 0.83 for BAL and non-BAL quasar sample respectively). This is qualatatively consistent with the results of Zhang et al., (2014).

It is well known that the blueshift of the C IV emission line in radio-quiet AGNs is, on average, stronger than in radio-loud AGNs (Marziani et al. 1996; Sulentic et al. 2000a; Richards et al. 2002, 2011). Statistically at least, the "radio-loud" objects are thought to have high black-hole masses and there is some form of radio-mode feedback (jet related) which is very different from the much more common (almost certainly wider opening-angle) outflow objects with large CIV-blueshifts.

So we find BALs have more hot dust, radio-loud have less. This is perfectly consistent with what we know about the positions of radio-loud objects and BALs in the C IV parameter space distribution (Richards et al., 2011).

Need to justify our use of model which has been optimised to fit colours of non-BAL quasars, when we know that BALs are typically redder.

What catalogue did we use to define quasar sample?

2.8 OTHER WORKS

Roseboom et al., (2013) studied a similar sample of luminous type 1 quasars. They, like us, modelled the NIR emission using a black-body and modelled the emission at longer wavelengths using a clumpy torus model. They find that while $L_{1-5\mu m}/L_{IR}$ appears relatively insensitive to L_{bol} and L_{IR}, a strong correlation appears between $L_{1-5\mu m}/L_{IR}$ and L_{IR}/L_{bol} (i.e. the dust covering factor). As the covering factor decreases, the maximum inclination at which a type 1 quasar would be seen increases. An increase in the inclination will mean direct sight lines to more of the inner wall of obscuring material closest to the accretion disc.

Mor and Trakhtenbrot, (2011) also looked at the hot dust properties of a sample of $0.75 < z < 2$ quasars, with photometry from SDSS and WISE. They modelled the NIR emission with hot clouds of pure graphite dust. They reported an anti-correlation between the covering factor of hot dust clouds and the quasar bolometric luminosity. Like us, they neglect cooler dust components which will dominate the SED at longer wavelengths. As we have discovered (see Figure residual plot), the missing flux decreases with redshift because we observe shorter rest-frame wavelengths when the observed spectrum is redshifted to a greater degree. This will induce an anti-correlation between the luminosity of the hot dust component and the luminosity of the quasar (which is correlated with redshift). At z=0.75, the W3 band-pass (the longest in their fits) is sensitive to flux from 6.9μm; at this wavelength we expect the contribution from cooler dust to dominate over the hot dust. It is possible that this effect could explain the tension with our own result that $R_{NIR/UV}$ does not depend on the quasar luminosity in our low-z sample.

Shen and Ho, (2014) quantify the relative torus emission using the $r - W1$ colour for a sample of $0.4 < z < 0.8$ SDSS quasars. At these redshifts W1 is observing between 1.9 and 2.4 microns in the rest-frame of the quasar, which suggests that they are sensitive to the same component of hot dust which we are investigating. They observe a mild trend of decreasing relative torus emission as the quasar luminosity increases. We note that their use of the r-W1 at much higher redshifts may be problematic, as the W1 flux will be increasingly dominated by direct emission from the accretion disc.

Gallagher et al., (2007) undertook a similar investigation for a much smaller sample of 234 radio-quiet quasars.

2.8.1 *Eddington ratio*

Wang et al., Zhang et al., and Mor & Trakhtenbrot find no significant dependence of the amount of hot dust on the Eddington ratio.

Shen & Ho find that torus emission is enhanced in quasars with larger R_{FeII}. They show how EW(OIII) and other high-ionisation lines (and to a lesser extent low-ionisation lines like MgII) anti correlate with R_{FeII}. The enhancement of torus emission relative to accretion disc emission at the high-RFeII end of EV1 may be caused by more efficient disc winds that facilitate the formation of a dusty torus. From our $z \sim 0.8$ composite SDSS spectra, we observed that objects with large NIR to UV luminosity ratios on average have stronger FeII emission.